Striatal output regulates the postnatal maturation of cortical circuits

Tara Deemyad[1,5*], Michael Janeček[1,2,*], Yi-Chun Shih[1,2], Vicente Valle[3], Andrew D'Agostino[1], Megan S. Perez[1,4], Kyle D. Ketchesin[1,2], Susana da Silva[3], Rui T. Peixoto[1,2]

1. Department of Psychiatry, University of Pittsburgh, 450 Technology Dr, Pittsburgh, PA 15219, USA
2. Center for Neuroscience at the University of Pittsburgh
3. Department of Ophthalmology, University of Pittsburgh, 1622 Locust St, Pittsburgh, PA 15219, USA
4. Department of Human Genetics, School of Public Health, University of Pittsburgh, Pittsburgh, USA.
5. Current address: Department of Otolaryngology, Johns Hopkins School of Medicine, 720 Rutland Ave, Baltimore, MD 21205, USA

* Authors contributed equally

Contact: peixotort@upmc.edu

Rui T. Peixoto is the lead author.

Abstract

The dorsomedial prefrontal cortex (dmPFC) is interconnected with the basal ganglia (BG) through large-scale circuit loops that regulate critical motor and cognitive functions. In mice, these circuits undergo extensive postnatal maturation with marked changes in neural activity and expansion of synaptic connectivity. While cortical activity is known to regulate the development of downstream striatal circuits, the role of the basal ganglia in cortical maturation remains unknown. Here, we used mesoscale two-photon microscopy and whole-cell electrophysiology to examine whether striatal output during early postnatal development impacts the maturation of upstream dmPFC circuits. We found that ablating spiny projection neurons of the direct or indirect pathways of the striatum during the first two postnatal weeks causes bidirectional changes in dmPFC neural activity, similar to what is observed in mature circuits. In addition, these manipulations alter the maturation of synaptic connectivity of dmPFC layer 2/3 pyramidal neurons, shifting the balance of excitation and inhibition of cortical circuits. These findings demonstrate that striatal output regulates the activity of cortical circuits during early postnatal development and suggest a regulatory role of the basal ganglia in the establishment of cortical circuits.

Introduction

The dorsomedial prefrontal cortex (dmPFC) and the basal ganglia (BG) are functionally interconnected through large-scale cortico-BG-thalamocortical (CBGT) circuits crucial for motor control and cognition[1–3]. The striatum is the largest input nucleus of the BG and the recipient of cortical and thalamic projections that synapse onto two classes of spiny projection neurons (SPN), which form functionally antagonistic output circuits termed direct (dSPN) and indirect (iSPN) pathways. In the mature brain, stimulation of dSPN or iSPN increases or suppresses cortical activity, respectively[4–6]. This bidirectional modulation of cortical activity is mediated by thalamic relay neurons whose activity is controlled by BG output nuclei and which in turn project to cortex, closing the loop of CBGT circuits [7–10]. In mice, CBGT circuits begin to develop in late embryonic stages and undergo a period of protracted maturation during the second and third postnatal weeks [11–14]. While considerable attention has been devoted to understanding how cortical activity regulates striatal development, the role of the striatum and the BG in the maturation of cortical circuits remains unclear. Nevertheless, the highly recurrent topology of CBGT circuits strongly couples cortical and BG activity[1,7,9,12,15–25], suggesting a potential role of the striatum in the development of cortical connectivity.

The postnatal maturation of cortical circuits involves extensive synaptic remodeling of excitatory glutamatergic pyramidal neurons (PYR) and inhibitory interneurons that release γ-aminobutyric acid (GABA). This process establishes an optimal balance of excitation and inhibition (E/I) and is strongly influenced by neural activity[26–29]. The role of experience and network activity in the maturation of local cortical circuits has been well studied in sensory cortical regions, where manipulations of peripheral or thalamocortical activity affect the maturation of glutamatergic and GABAergic synaptic connectivity[30–35]. Furthermore, the maturation of GABAergic interneurons plays a pivotal role in synaptic plasticity mechanisms associated with critical periods of cortical development[23,36–42]. This maturation is accompanied by a transition in network activity patterns from sporadic events of synchronized activity to decorrelated high-frequency activity of sparse neuron populations [43–48]. The activity-dependent mechanisms regulating the postnatal maturation of dmPFC circuits are comparatively less understood than those in sensory cortical areas, partly due to the absence of direct sensory input in frontal cortical regions. However, both dmPFC PYR and GABAergic interneurons are major targets of BG-recipient thalamic nuclei[49–51], and manipulations of thalamocortical activity during postnatal development significantly affect their maturation[23,36–38].

The initial wiring of CBGT circuits is established perinatally during a period of extensive corticostriatal and thalamocortical innervation. However, the majority of synaptic connectivity within these circuits only matures during the second postnatal week, coinciding with the onset of sensory experience. Notably, during this stage, mature patterns of neural activity emerge simultaneously in cortical, thalamic, and BG circuits, suggesting that the postnatal development of CBGT circuits is a concerted process governed by activity-dependent mechanisms. Moreover, the maturation of corticostriatal and thalamocortical synapses is strongly influenced by network activity, with elevated activity promoting and lower activity suppressing synaptogenesis[12–14,52,53]. Interestingly, silencing striatal iSPN or dSPN output during postnatal

development can either increase or decrease the maturation of glutamatergic afferents targeting the striatum. These manipulations induce similar effects in both types of SPNs and are not caused by cell-autonomous mechanisms, suggesting that they emerge from changes in overall network activity caused by early dSPN-iSPN imbalances[54]. Based on this evidence, we hypothesized that dSPN and iSPN already modulate cortical activity during early postnatal development and that network activity changes mediated by the BG play a regulatory role in the postnatal maturation of cortical circuits.

Results

To investigate the influence of striatal circuit output on cortical activity during postnatal development, we selectively ablated either dSPN or iSPN during the first two postnatal weeks and assessed their impact on dmPFC neurons *in vivo* at postnatal day (P) 13-16 using two-photon microscopy. Given that BG output nuclei project to the cortex through strictly ipsilateral thalamic relay pathways [20,22], we performed unilateral ablations of SPN and monitored neural activity in dmPFC regions of both cerebral hemispheres simultaneously **(Figure 1A and supplemental video 1)**. This approach allowed for within-animal comparisons of dmPFC activity in manipulated and control hemispheres, mitigating variability from the fast maturation of synaptic and intrinsic properties during this postnatal period [12,44,46–48,55]. We targeted ablations to dorsomedial striatum (DMS) as it is the striatal region receiving most extensive projections from dmPFC. To ablate dSPN or iSPN we injected an adeno-associated virus (AAV) expressing Caspase3 in a Cre-dependent manner (AAV5-DIO-taCasp3-TEVp) unilaterally in DMS of Drd1a-Cre (D1-Cre) or Adora2A-Cre (A2A-Cre) transgenic mice[56], respectively (**Figure 1B**). To monitor neural activity in cortical circuits, we bilaterally injected AAV9-hSyn-GCaMP8s in dmPFC. Injections were performed at P1 to maximize cortical GCaMP8s expression and induce Caspase3 during a period of natural ongoing apoptosis in the striatum[57,58]. Spike-related calcium (Ca^{2+}) fluorescence of GCaMP8s expressing neurons was measured at P13-P16 (**Figures 1C-1E**) and transients recorded in both hemispheres were analyzed using Suite2P (see methods)[59]. AAV-DIO-Casp3 injection at P1 induced a 31% reduction in the number of DMS Cre^{+} SPNs, quantified by mRNA in situ hybridization against Dopamine Receptor 1 (D1R) and D2R, which are predominantly expressed in dSPN and iSPN, respectively (**Figures 1F-H** $D2R^{+}$/DAPI Control = 176.4 ± 24.6 nuclei; Casp3 = 178.2 ± 31.4 nuclei; $D1R^{+}$ /$DAPI^{+}$ Control = 184.9 ± 24.6 nuclei; Casp3 = 128 ± 9.5 nuclei, n = 9 paired slices from 3 mice; Wilcoxon matched-pairs rank test, p = 0.91 and p = 0.0195). Loss of function of iSPN and dSPN>iSPN activity imbalances are associated with numerous neurodevelopmental and psychiatric disorders, prompting us to investigate how postnatal ablation of iSPN in A2A-Cre mice affects cortical activity. Interestingly, we observed a consistent increase in the average GCaMP8s transient amplitude in dmPFC neurons of the Caspase3-injected hemisphere compared to the control side (**Figures 2B-D**, $\Delta F/F$ average amplitude: Control = 0.078 ± 0.009, Casp3 = 0.11± 0.012, n= 17 recordings from 8 mice, Unpaired *t*-test p=0.036). To control for variable number of regions of interest (ROI) analyzed per mouse we calculated the cumulative distribution function (CDF) of $\Delta F/F$ amplitude by randomly sampling similar number of ROIs from each group. This analysis showed a similar increase in the distribution of transient amplitude in dmPFC neurons

of the injected hemisphere, confirming that loss of iSPN increases cortical neuron (**Figures 2D,** KS-distance = 0.19, *p* <0.0001, Kolmogorov-Smirnov test). We also observed elevated average ΔF/F transient frequency in neurons of the iSPN-ablated hemisphere (**Figures 2E-F,** ΔF/F transient frequency: Control = 0.031 ± 0.003 Hz, Casp3 = 0.046 ± 0.004 Hz, p = 0.013, n = 17 recordings from 8 mice, Unpaired *t*-test). CDF of inter-event interval (IEI) confirmed elevated levels of neural activity in dmPFC neurons following iSPN ablation (**Figures 2G,** KS-distance = 0.14, *p* <0.0001, Kolmogorov-Smirnov test). The postnatal maturation of cortical activity patterns is characterized by a sparsification of neural activity [43–48]. Interestingly, increases in overall activity levels following iSPN ablation were accompanied by a reduction in pairwise correlation of ΔF/F signal, when compared to neurons of the contralateral control hemisphere (**Figures 2H-J**, Neuron pairs correlated: Control = 21.8 ± 1.3 %, Casp3 = 17.3 ± 1 % in perturbed hemisphere, p=0.01; unpaired *t*-test). Together, these findings indicate that loss of iSPN during early postnatal development increases neural activity and reduces neural synchrony.

Activation of dSPN and iSPN induces an opposing modulation of cortical circuits in adult mice. To test whether this bidirectional modulatory effect is already established during postnatal development we ablated dSPN using a similar experimental approach in D1-Cre mice (**Figure 3A**). Contrary to our findings in A2A-Cre mice, ablation of dSPN decreased the frequency and amplitude of Ca^{2+} transients in neurons of the Casp3 injected hemisphere compared to control (**Figures 3B-G**, ΔF/F average amplitude: Control = 0.08 ± 0.01, Casp3 = 0.13 ± 0.02, p=0.03; ΔF/F average frequency: Control = 0.07 ± 0.01 Hz, Casp3 = 0.04 ± 0.01 Hz, p = 0.001; Mean IEI: Control = 6.4 ± 0.8 sec, Cre = 12.7± 1.8 sec, p = 0.002, n = 18 recordings from 7 mice. Unpaired *t*-test). Further analysis of the CDF of average ΔF/F amplitude of all ROI for each group showed a similar difference in the distribution between neural activity of Casp3 injected and control side, confirming that loss of dSPN decrease ΔF/F amplitude (**Figures 3D,** distance = 0.23, *p* <0.0001, Kolmogorov-Smirnov test). In addition, CDF of IEI confirmed elevated levels of neural activity in dmPFC neurons following dSPN ablation (**Figures 3G** distance=0.06, *p* <0.0001, Kolmogorov-Smirnov test). Interestingly, loss of dSPN increased pairwise correlation of neural activity in dmPFC (**Figure 3H-J**, Neuron pairs correlated: Control = 16.5 ± 1.2%, Casp3 = 25.2 ± 1.9%, p=0.0004 unpaired t-test, CDF: distance=0.21, *p* <0.0001, Kolmogorov-Smirnov test). These results indicate that dSPN and iSPN ablation during postnatal development induce opposing effect in the overall level and synchrony of dmPFC neural activity.

To investigate whether striatal-induced changes in cortical activity alter the maturation of synaptic connectivity in dmPFC circuits, we recorded AMPAR-mediated miniature excitatory postsynaptic currents (mEPSCs) and GABA-mediated miniature inhibitory postsynaptic currents (mIPSCs) from dmPFC L2/3 PYR from the same hemisphere subjected to Caspase3 injection in DMS. In A2A-Cre mice, the frequency of mEPSCs was not affected by the loss of iSPN (**Fig. 4A-B**; mEPSC frequency: control = 1.84 ± 0.206 Hz, *n* = 36 cells from 4 mice; A2A-Cre = 1.70 ± 0.175 Hz, *n* = 30 cells from 3 mice; Mann-Whitney test, *p* = 0.863). However, loss of iSPN resulted in a striking reduction of mIPSC frequency (**Fig. 4C**; mIPSC frequency: control = 0.95 ± 0.066 Hz, *n* = 36 cells from 4 mice; A2A-Cre = 0.61 ± 0.050 Hz, *n* = 32 cells from 3 mice; Mann-Whitney test, *p* < 0.0001). This mean difference was corroborated by CDF of individual IEIs sampled across PYRs, indicating that loss of iSPN reduces GABAergic synaptic inputs onto

PYR (**Supplementary Fig. 1G**; CDF of mIPSC IEIs: KS-distance = 0.177, $p < 0.0001$). Interestingly, within-neuron mEPSC/mIPSC frequency ratio was increased in A2A-Cre mice compared to controls (**Fig. 4D**; E/I frequency ratio: control = 2.12 ± 0.204, n = 33 cells from 4 mice; A2A-Cre = 3.16 ± 0.364, n = 30 cells from 3 mice; Mann-Whitney test, p = 0.021). This E/I deficit arises from reduction of the frequency of mIPSCs compared to mEPSCs as received by the same neuron (**Fig. 4E**; Robust linear regression: control slope = 0.17 ± 0.050, CI95% [0.070, 0.268], p < 0.001; A2A-Cre slope = 0.018 ± 0.035, $CI_{95\%}$ [-0.051, 0.086], p = 0.615).

The amplitude of mEPSCs between PYR of control and A2A-Cre animals was similar (**Fig. 4F**; mEPSC amplitude: Control = 10.49 ± 0.196 pA, n = 36 cells from 4 mice; A2A-Cre = 10.75 ± 0.187 pA, n = 30 cells from 3 mice; Mann-Whitney, p = 0.156), suggesting normal postsynaptic receptor density and quantal content. However, loss of iSPNs induced a slight decrease in amplitude of GABA-mediated mIPSCs (**Fig. 4G**; mIPSC amplitude: control = 12.43 ± 0.426 pA, n = 36 cells from 4 mice; A2A-Cre = 11.39 ± 0.502 pA, n = 32 cells from 3 mice; Mann-Whitney, p = 0.054) that was corroborated by bootstrapped CDF (**Supplementary Fig. 1H**; CDF of mIPSC amplitude: Kolmogorov-Smirnov distance = 0.099, $p < 0.0001$). Ratio of mEPSC amplitude did not differ as a result of iSPN ablation (**Fig. 4H**; E/I amplitude ratio: control = 0.898 ± 0.036, n = 33 cells from 4 mice; A2A-Cre = 0.986 ± 0.046, n = 30 cells from 3 mice; Mann-Whitney, p = 0.177) and regression analysis revealed null relationship between mEPSC/mIPSC amplitude (**Fig. 4I**; Robust linear regression: control slope = -0.300 ± 0.432, $CI_{95\%}$ [-1.146, 0.546], p = 0.487; A2A-Cre slope = -0.328 ± 0.454, $CI_{95\%}$ [-1.217, 0.562], p = 0.470). Finally, we did not detect differences in passive intrinsic properties (**Supplementary Fig. 1B-D**) or miniature current kinetics between dmPFC neurons of both groups (**Supplementary Fig. 1I-L**).

Similar to iSPN ablation, mEPSC frequency of L2/3 PYR of D1-Cre mice was normal (**Fig. 4K**; mEPSC frequency: control = 2.367 ± 0.308 Hz, n = 29 cells from 3 mice; D1-Cre = 2.697 ± 0.218, n = 35 cells from 3 mice; Mann-Whitney, p = 0.059). However, mIPSC was not affected by the loss of dSPN (**Fig. 4L**; mIPSC frequency: Control = 1.372 ± 0.125 Hz, n = 28 cells from 3 mice; D1-Cre = 1.214 ± 0.077 Hz, n = 35 cells from 3 mice; Mann-Whitney, p = 0.569). Nonetheless, the within-neuron mEPSC/mIPSC frequency ratio was significantly elevated (**Fig. 4M**; E/I frequency ratio: Control = 1.752 ± 0.148, n = 28 cells from 3 mice; D1-Cre = 2.207 ± 0.171, n = 35 cells from 3 mice; Mann-Whitney, p = 0.032), suggesting that optimal striatal activity is required for proper maturation of cortical E/I balance. Despite the slight E/I increase, regression of mini frequency revealed a significantly positive relationship of mEPSCs and mIPSCs in both control and manipulated groups (**Fig. 4N**) (Robust linear regression: Control slope = 0.2296 ± 0.049, $CI_{95\%}$ [0.134, 0.325], p < 0.001; D1-Cre slope = 0.2108 ± 0.052, $CI_{95\%}$ [0.108, 0.313], p < 0.001).

No difference was detected in the amplitudes of both mEPSC (**Fig. 4O**; mEPSC amplitude: Control = 11.26 ± 0.157 pA, n = 29 cells from 3 mice; D1-Cre = 11.08 ± 0.194 pA, n = 35 cells from 3 mice; Mann-Whitney, p = 0.421) and mIPSCs (**Fig. 4P**; mIPSC amplitude: Control = 1.372 ± 0.125 pA, n = 28 cells from 3 mice; D1-Cre = 1.214 ± 0.077 pA, n = 35 cells from 3 mice; Mann-Whitney, p = 0.5685) consistent with the comparable mEPSC/mIPSC amplitude ratio between groups (**Fig. 4Q**; E/I amplitude ratio: Control = 0.848 ± 0.029, n = 28 cells from 3 mice; D1-Cre = 0.788 ± 0.022, n = 35 cells from 3 mice; Mann-Whitney, p = 0.1015). Regression of current

amplitude indicates that there is no linear relationship in the size of mEPSCs and mIPSCs in either group (**Fig. 4R**; Robust linear regression: control slope = -0.6967, $CI_{95\%}$ [-1.496, 0.103], p = 0.09; D1-Cre slope = 0.126, $CI_{95\%}$ [-0.483, 0.735], p = 0.406). Except for membrane capacitance, which was decreased in PYR following dSPN ablation, intrinsic properties and mEPSC current kinetics were not affected by dSPN ablation (**Supplementary Fig. 2;** Control = 59.68 ± 2.33 pF, n = 30 cells from 3 mice; D1-Cre = 53.89 ± 2.07 pF, n = 36 cells from 3 mice; Mann-Whitney, p = 0.033).

Discussion

These results demonstrate that imbalances in striatal output during postnatal development alter the activity of dmPFC circuits. This early modulation of network activity by the striatum is consistent with previous findings, where postnatal silencing of dSPN or iSPN either decreased or increased striatal glutamatergic connectivity, respectively [54]. This effect was not replicated by cell-autonomous silencing of SPN, suggesting that it might be driven by global changes in network activity resulting from dSPN-iSPN imbalances. Our findings support this hypothesis, showing that the bidirectional modulation of cortical circuits by dSPN and iSPN, typically observed in mature stages, is already established during early postnatal development[4–6]. These results are also significant in the clinical context, as abnormal maturation of corticostriatal circuits has emerged as a common pathophysiology associated with neurodevelopmental disorders such as ASD, schizophrenia, and attention-deficit/hyperactivity disorder [60–64]. The cortical hyperactivity induced by partial ablation of iSPN is particularly relevant, considering that dSPN>iSPN activity imbalances are observed in numerous human disorders and mouse models of ASD[65–68]. These findings suggest that CBGT circuits are not able to compensate for postnatal loss of SPN, reinforcing the notion that disrupted striatal circuit maturation is a relevant pathogenic mechanism that can lead to abnormal activity patterns across the brain. Besides increasing the amplitude and frequency of Ca^{2+} transients, loss of iSPN also decreased pairwise correlation between PYR activity. This finding is intriguing in light of the significant developmental transition in cortical activity patterns that occurs during the second postnatal week, shifting from periods of discontinuous highly synchronous activity to the high-frequency sparse activity characteristic of mature circuits[44,46]. While cortical processes such as the development of GABAergic inhibition might also regulate the maturation of cortical activity patterns during this period, these findings suggest a potential involvement of the striatum and the BG in this process. Indeed, neurons of the globus pallidus and substantia nigra exhibit asynchronous rhythmic activity that are thought to actively decorrelate neural activity across CBGT networks[69,70]. Disruption of this network mechanism in neurodegenerative diseases such as Parkinson's and Huntington's diseases generates pathological brain oscillations that initially manifest in the BG and subsequently spread to the cortex[71–74]. Thus, BG modulation of cortical circuits might contribute to the sparsification of cortical activity patterns observed during postnatal development [43–48].

Ablation of iSPN altered the maturation of L2/3 PYR dmPFC synaptic connectivity, leading to a pronounced reduction in mIPSC frequency and a corresponding elevation of PYR E/I synaptic

balance. This result suggests a possible role of BG activity in the development of cortical inhibitory circuits. Indeed, thalamocortical projections originating from BG-recipient thalamic nuclei synapse onto various classes of cortical interneurons[49,50]. These projections are observed in the upper cortical plate perinatally and reach peak density in L2/3 dmPFC around P10. In sensory cortical regions, manipulations of sensory input or thalamocortical drive strongly influence the development of cortical GABAergic interneurons[23,36–38], suggesting that mechanisms that alter the activity of dmPFC projecting thalamic nuclei might induce a similar effect. The adaptations in interneuron maturation caused by changes in network activity are complex and depend on the specific cortical region, neuronal cell type and developmental timing [75]. Our findings indicate that cortical hyperactivity induced by iSPN ablation during the first two postnatal weeks reduces cortical inhibition, suggesting a non-homeostatic adaptive response. Conversely, we observed no reduction of cortical inhibition following dSPN ablation. However, both manipulations led to an increase in E/I balance, albeit through different mechanism. While iSPN ablation strongly reduced mIPSCs, the elevated E/I balance following loss of dSPN resulted from a partial increase in mEPSC frequency. Nevertheless, the ablation of dSPN significantly reduced cortical activity and increased pairwise correlations of PYR Ca^{2+} transients, further supporting the bidirectional role of dSPN and iSPN activation over cortical activity and circuit maturation [4–6].

From a developmental perspective, early modulation of cortical activity by the striatum suggests a potential role of the BG in shaping cortical circuit development. The experience-dependent maturation of cortical circuits is considered a key factor in the remarkable adaptability of humans and other mammals during development[39]. However, the specific mechanisms that translate early experiences into dmPFC circuit maturation remain elusive. Dopamine-induced striatal circuit plasticity regulates reinforcement and value-based learning[15,76]. Dopamine alters the balance of dSPN and iSPN activity due to differential expression of D1R and D2R dopamine receptors in the two SPN populations, that respectively increase or decrease neuronal excitability[15]. Notably, during postnatal development, dopamine signaling promotes glutamatergic synaptogenesis in dSPN but not in iSPN, resulting in a bias towards dSPN>iSPN connectivity[13]. Our results show that the balance between dSPN and iSPN activity during this period influences activity patterns and the maturation of synaptic connectivity in dmPFC, suggesting that early modulation of striatal circuits by dopamine or other plasticity mechanisms could influence prefrontal cortical maturation. This potential role of the striatum in mediating cortical plasticity is consistent with a recent study showing that striatal activity is required for the initial establishment, but not subsequent control, of volitional intracortical modulation required for the control of brain-machine interfaces[77]. Additionally, while the striatum and the dmPFC are critical for reward-based reinforcement learning in adults, the specific contributions of these two structures in this process remain unclear[78]. If the striato-cortical regulation of cortical connectivity described here extends beyond postnatal periods, it might provide a mechanistic link between dopamine-related plasticity processes in the striatum and structural changes in prefrontal circuits associated with reinforcement learning. Finally, cortical GABAergic dysfunction and deficits in striatal circuits are prevalent in numerous neurodevelopmental and psychiatric disorders. Our results raise the possibility that these two pathophysiological

abnormalities could be causally related, and that early interventions that normalize striatal activity might ameliorate cortical inhibition deficits in some conditions.

Acknowledgements

We thank Lars Nelson for programming Clampsuite, which we used for electrophysiology data analysis. We thank Sidney Dawkins, Lan Chen, Tasha Merchant, and Michael Matarazzo for technical assistance and management of the mouse colony. We thank Susanne Ahmari for providing the Adora2A-Cre and Drd1-Cre transgenic mice. We thank Muhammad Nazir for helping with microscope maintenance and troubleshooting. This project was supported by R.P. grant R01MH124695 and Simons Foundation Bridge to Independence award. K.D.K. was supported by K01MH128763 and the Brain and Behavior Research Foundation (30823; P&S Fund).

Author Contributions

T.D. collected and analyzed the imaging data; M.J. and Y.S. collected electrophysiology data; M.J. analyzed the electrophysiology data; M.J. and A.D.A. performed mouse genotyping and intracranial viral injections; M.S.P. and K.D.K. performed the RNAScope *in situ* hybridizations; V.V and S.S. analyzed in situ hybridization data; T.D., M.J. and R.T.P wrote and edited the manuscript; R.P. conceived the study and supervised the experiments.

Declaration of interests

The authors declare no competing interests.

Figure Legends

Fig. 1. Bilateral imaging of dmPFC activity during postnatal development using two-photon microscopy. (A) Diagram illustrating mouse CBGT circuit,s highlighting the bidirectional modulation of cortical activity by dSPN and iSPN. **(B)** Experimental approach of two-photon microscopy experiments: bilateral injection of AAV-hSyn-GCaMP8s in the dmPFC of both hemispheres and unilateral injection of AAV-DIO-Caspase3 in DMS at P0-P1, followed by cortical imaging at P13-P16. **(C)** Bilateral recordings of dmPFC neural activity in the left and right hemispheres. Scale bar: 200 μm **(D)** ROI segmentation and **(E)** respective ΔF/F activity of GCaMP8s expressing cortical neurons. Scale bars: 10 sec / 0.2 ΔF/F **(F)** Coronal section and **(G)** magnified view of the quantification of D1R and D2R expression in DMS by RNAScope *in situ* hybridization. Scale bars: 1 mm and 200 μm. **(H)** Quantification of D1R and D2R expressing cells in DMS at P15 following AAV-DIO-Caspase3 injection at P1. GPe- Globus Pallidus externus, STN- Subthalamic nucleus, SNr – Substantia Nigra pars reticulata, Thal- Thalamus.

Fig. 2. Postnatal ablation of iSPN increases dmPFC neural activity. (A) Schematic of bilateral two-photon imaging of GCaMP8s (green) activity in dmPFC at P15 following unilateral ablation of iSPN in the DMS at P1 using AAV-DIO-Caspase3 (red) injection in A2A-Cre mice **(B)** Raster plots of GCaMP8s Ca^{2+} transients in dmPFC neurons of control (left) and Caspase3 injected (right) hemispheres **(C)** Mean GCaMP8s $\Delta F/F$ Ca^{2+} transient amplitude of dmPFC neurons recorded in control and Caspase3 injected hemisphere of each recording. Paired data points represent average neural data recorded in the same session. **(D)** CDF of Ca^{2+} transient amplitude from neurons of both hemispheres. **(E)** Mean GCaMP8s $\Delta F/F$ Ca^{2+} transient frequency and **(F)** Normalized Ca^{2+} transient amplitude and frequency of control and manipulated dmPFC hemispheres for each recording. **(G)** CDF of mean IEI of Ca^{2+} transients from neurons of both hemispheres. **(H)** Pearson coefficients from pairwise comparisons of GCaMP8s $\Delta F/F$ Ca^{2+} traces of dmPFC neurons in control and DMS Caspase3 injected hemispheres. **(I)** Percent of ROI pairs with significant correlated activity **(J)** CDF of correlation coefficients. All values are reported as mean ± SEM

Fig. 3. Postnatal ablation of dSPN decreases dmPFC neural activity. (A) Schematic of bilateral two-photon imaging of GCaMP8s (green) activity in dmPFC at P15 following unilateral ablation of dSPN in DMS at P1 using AAV-DIO-Caspase3 (red) injection in D1-Cre mice **(B)** Raster plots of of GCaMP8s Ca^{2+} transients in dmPFC neurons of control (left) and Caspase3 injected (right) hemispheres **(C)** Mean GCaMP8s $\Delta F/F$ Ca^{2+} transient amplitude of dmPFC neurons recorded in control and Caspase3 injected hemisphere of each recording. Paired data points represent average neural data recorded in the same session. **(D)** CDF of Ca^{2+} transient amplitude from neurons of both hemispheres. **(E)** Mean GCaMP8s $\Delta F/F$ Ca^{2+} transient frequency and **(F)** Normalized Ca^{2+} transient amplitude and frequency of control and manipulated dmPFC hemispheres for each recording. **(G)** CDF of mean IEI of Ca^{2+} transients of neurons of both hemispheres. **(H)** Pearson coefficients from pairwise comparisons of GCaMP8s $\Delta F/F$ Ca^{2+} traces of dmPFC neurons in control and DMS Casp3 injected hemispheres. **(I)** Percent of ROI pairs with significant correlated activity **(J)** CDF plots of correlation coefficients. All values are reported as mean ± SEM

Fig. 4. Loss of iSPN but not dSPN reduces GABAergic drive in dmPFC PYR. (A) Left: Schematic of whole-cell voltage-clamp recordings in PYR of L2/3 dmPFC in P14-15 acute brain slices of control (black) or A2A-Cre^{+} (red) mice neonatally injected with AAV-DIO-Caspase3 (grey). Center: Representative AMPAR-mediated mEPSCs recorded in voltage-clamp (V_h = -70 mV) in PYR of L2/3 dmPFC ipsilateral to the Caspase3 injection in control or A2A-Cre^{+} manipulated mice. Right: GABA-mediated mIPSCs recorded in voltage-clamp (V_h = 0 mV) in same neurons **(B)** Mean frequency of AMPAR-mediated mEPSCs and **(C)** GABA-mediated mIPSCs recorded in L2/3 dmPFC PYR of control (grey) animals and A2A-Cre^{+} (red) animals. Note that loss of iSPNs in the A2A-Cre^{+} condition results in ~25% decrease of mIPSC input. **(D)** Mean mEPSC/mIPSC frequency ratio of L2/3 dmPFC PYR sampled from control (grey) and A2A-Cre^{+} (red) animals **(E)** Robust linear regression of mEPSC and mIPSC frequency in L2/3 dmPFC PYR of control (grey) and A2A-Cre^{+} (red) animals indicates that linear scaling of excitatory and inhibitory input is disrupted by postnatal loss of iSPNs. **(F)** Mean amplitude of

AMPAR-mediated mEPSCs and **(G)** GABA-mediated mIPSCs in PYR of control (grey) and A2A-Cre$^+$ (red) animals. **(H)** Mean mEPSC/mIPSC amplitude ratio of L2/3 dmPFC PYR sampled from control (grey) and A2A-Cre$^+$ (red) animals. **(I)** Robust linear regression of mEPSC and mIPSC amplitude in L2/3 dmPFC PYR of control (grey) and A2A-Cre$^+$ (red) animals. **(J)** Left: Schematic of whole-cell voltage-clamp recordings in PYR of L2/3 dmPFC in P14-15 acute brain slices of control (black) or D1-Cre$^+$ (blue) mice neonatally injected with AAV-DIO-Caspase3 (grey) in DMS. Center: Representative AMPAR-mediated mEPSCs recorded in voltage-clamp (V_h = -70 mV) in PYR of L2/3 dmPFC ipsilateral to the Caspase3 injection in control (grey) or D1-Cre$^+$ (blue) mice. Right: GABA-mediated mIPSCs recorded in voltage-clamp (V_h = 0 mV). **(K)** Mean frequency of AMPAR-mediated mEPSCs and **(L)** GABA-mediated mIPSCs recorded in L2/3 dmPFC PYR of control (grey) and D1-Cre$^+$ (blue) animals. **(M)** Mean mEPSC/mIPSC frequency ratio of L2/3 dmPFC PYR sampled from control (grey) and D1-Cre$^+$ (blue) animals **(N)** Robust linear regression of mEPSC and mIPSC frequency in L2/3 dmPFC PYR of control (grey) and D1-Cre$^+$ (blue) animals. **(O)** Mean amplitude of AMPAR-mediated mEPSCs and **(P)** GABA-mediated mIPSCs in PYR of control (grey) and D1-Cre$^+$ (blue) animals. **(Q)** Mean E/I amplitude ratio of L2/3 dmPFC PYR sampled from control (grey) and D1-Cre$^+$ (blue) animals. **(R)** Robust linear regression of mini amplitude in L2/3 dmPFC PYR of control (grey) and D1-Cre$^+$ (blue) animals. All values are reported as mean ± SEM except for linear regression results described by slope ± standard error.

Experimental model and subject details

Animals

All procedures were conducted in accordance with protocols approved by the University of Pittsburgh Institutional Animal Care and Use Committee (IACUC) and adhered to the Guide for the Care and Use of Laboratory Animals published by the National Institutes of Health. Naive C57BL/6J mice were mated with transgenic mice expressing Cre Recombinase under the control of either Dopamine receptor type-1 promoter (Tg(Drd1a-cre)EY262Gsat/Mmcd) or the Adenosine-2a receptor promoter (A2A-cre (Tg(Adora2acre)KG139Gsat)[56]. Same-age littermate comparisons were performed when possible and litter size was capped at eight pups to minimize variability in developmental rates. Mice were housed in a facility maintained at constant temperature and 12/12h light/dark cycle and had *ad libitum* access to water and food. All the experiments were conducted during the light phase of the cycle.

Stereotaxic virus injection

Adeno-associated viruses used in this study are commercially available (Addgene, MA, USA) pGP-AAV1-syn-jGCaMP8s-WPRE (Addgene #162379), and pAAV5-flex-taCasp3-TEVp (#45580, lot #143244). Viruses were aliquoted and stored at -80°C. Virus titers were ≥ 1×10^{13} and ≥ 7×10^{12} GC/mL, respectively. Viral injections were performed on neonatal pups (P0-P1) under hypothermia-induced anesthesia. Briefly, pups were cooled on ice-cold aluminum for approximately 5 minutes. The pups were then transferred to a cooled stereotaxic platform (WPI, #502600) neonatal adaptor and maintained at consistently low temperature using a dry ice

pellet submerged in 100% ethanol. Toe pinch extensor reflex was monitored as an indicator of distress and depth of anesthesia. After achieving proper stereotaxic positioning, guided by midline and eye-ear distance coordinates, a glass pipette with approximately 30 μm tip in diameter containing the virus was carefully lowered through the skin and skull using a stereotaxic manipulator (Kopf). Injections targeted the dmPFC (centered at [from Lambda] AP: +2.5 mm, ML: ±0.4 mm, DV: +0.7 mm) or the DMS (AP: +2.1 mm, centered at [from Lambda] ML: -1 mm or +1 mm, DV: +1.7 mm). Injection volume was 200 nL and rate of injection 50 nL/min speed. After the injection, the glass pipette was left in place for three minutes to allow virus to diffuse. Pups were then immediately placed on a heat pad to return to physiological temperatures and subsequently returned to their home cage. Animals were allowed to recover until the day of imaging (P13-P16).

Stereotaxic window surgery

At P13-P16, mice were fully anesthetized with isoflurane ensuring unresponsiveness to toe pinch as a sign of distress and depth of anesthesia. The head fur was shaved with hair remover (Nair) and the skin was cleaned with three cycles of alternate Betadine and ethanol wipes. The skin was incised with a scalpel and the soft tissues reflected laterally by blunt dissection. Once a small region of the skull was exposed the bone surface was dried with cotton swabs and compressed air prior to performing the craniotomy and implanting the cranial window. A ~3mm craniotomy was performed on the surface of the skull above the brain region of interest using sterile carbide drill bits (Microscopy Dental). The skull flap was gently removed using a pair of fine forceps without damaging the underlying dura. A glass coverslip (3-4 mm round #0, 0.1 mm, Warner instruments) was lowered on top of the brain and glued with Loctite 454 glue. A thick layer of medical grade bacteriostatic dental cement (C&B Metabond®) was then applied to seal the edge of the window to the surrounding skull. A titanium headplate was implanted and attached to the skull using dental cement with an orthogonal orientation in relation to the window. All areas of exposed skull were covered with dental cement. Mice were administered ketoprofen and allowed to recover for three hours before imaging.

Two-photon imaging

Images were acquired using a resonant scanning two-photon microscope (Ultima 2P plus, Bruker, WI) at 8 Hz frame rate and 1024x1024 pixel resolution through a 16x water immersion lens (Nikon 16x 0.8NA). dmPFC was imaged at a depth between 150 and 250 μm, at the level of cortical layer 2/3. Excitation light was provided by tunable femtosecond infrared source (920 nm) wavelength laser (Insight X3, Spectra-Physics, CA). Tunable wavelength beams were combined with a dichroic mirror (ZT1040dcrb-UF3, Chroma, VT) before being routed to the microscope's galvanometers. PrairieView software (vX5.5 Bruker, WI) was used to control the microscope. Fields of view were selected based on GCaMP expression. Multiple imaging sessions were acquired from each cranial window at varying depths. Images were collected while mice were alert and head restrained inside an acrylic tube on top of a heat pad at 37C. Individual imaging sessions were approximately 30 minutes in duration.

Imaging Data Analysis

Images of GCaMP8s fluorescence collected with 920 nm excitation were processed in Suite2p (v 0.10.3, Cellpose 0.7.3). Image sequences were registered, and motion corrected. Regions of interests (ROIs) were identified based on functional segmentation based on correlation of pixel intensity across time. The measured fluorescence signal at each time point (F(t)) was calculated by subtracting the fluorescence of the neuropil (F_{neu}) surrounding the cell body from the fluorescence of the cell body (F), weighted by a factor of 0.7 ($F(t) = F - 0.7*F_{neu}$). For each ROI we calculated $\Delta F/F = (F(t) – F(0))/F(0)$, where F(0) was calculated by a rolling percentile to find the 8th percentile of F(t) from 150 frames before each data point. To identify calcium events, a threshold of one standard deviation (SD) above F(0) was chosen. Additionally, we excluded events with peaks above threshold for less than 500ms based on GCaMP8s decay kinetics. The time of the peak of each event was detected using a prominence based peak finding algorithm and used to calculate peak amplitude and inter-event intervals (ISI) and frequency of events for each ROI. Example raster plots of events for all ROIs in a movie are shown in Figures 2B and 3B. ISI and amplitudes were averaged for each ROI in each recording session (e.g., shown as CDF plots in Figs. 2D and 2G) and for all ROIs in that movie (e.g., shown as points in Figs. 2C, 2E and 2F). We calculated the pairwise linear correlation coefficient between ROIs in each recording using Pearson correlation of ΔF/F traces. To determine the threshold for identifying synchronous activity based on the calculated correlation coefficients, we randomly shuffled event times for each ROI to generate ROIs that have no correlation in activity (i.e., random activity for each ROI). We then calculated the correlation coefficients for pairs of ROIs. We used 1000 repetitions of random shuffling and calculation of correlation coefficients to generate a distribution of correlation coefficients for 'uncorrelated' ROIs. The 99th percentile of this distribution was considered as the threshold for identifying synchronous activity (i.e., $p < 0.01$). Examples of correlation coefficients between pairs of ROIs (i.e., x and y axes) that are above threshold are plotted in Figs. 2H and 3H. Percent of ROI pairs with significant correlated activity (i.e., above threshold) are reported for the two sides for each movie (e.g., Fig. 2I) and CDF plots of these correlation coefficients are also shown (e.g., Fig. 2J). All pairwise comparisons of mean values across datasets were done with unpaired t-test or two-sample Kolmogorov-Smirnov test in Matlab. Comparisons performed directly on classification results were done with unpaired permutation (i.e., randomization) tests with 10,000 iterations, where $p<.0001$ indicates the highest significance for the number of runs performed.

In situ hybridization

RNAscope *in situ* hybridization was performed on fresh frozen striatal tissue sections collected from D1-Cre or A2A-Cre mice injected into one hemisphere of the striatum with AAV5-DIO-taCasp3-TEVp. Brains were sectioned in a cryostat at 14um depth to isolate DMS containing sections. The left hemisphere was fiducially labeled to identify the injected hemisphere during image processing. Tissue sections were mounted onto slides and processed according to the RNAscope Multiplex Fluorescent Reagent Kit v2 protocol (UM 323100) using the following probes: D1 (RNAscope™ Probe- Mm-Drd1, cat# 461901) and D2 (RNAscope™ Probe- Mm-Drd2-C2, cat# 406501-C2). Sections were imaged at 20x magnification using an Olympus

SLIDEVIEW VS200 research slide scanner. TIFF files were analyzed in the open-source software Qupath (version 0.4.4), where two GeoJSON objects encompassing the left and right striatum were traced and used on all of the sections; DAPI, FITC and CY5 channels were then isolated from these specific regions. The total number of nuclei per striatum was obtained by manually counting the DAPI channel using the count tool in Adobe Photoshop, while the FITC and Cy5 signals were segmented on Qupath by using the "dsb2018_heavy_augment.pb" pretained model of the StarDist extension. The resulting masks were then saved as rendered SVG files, converted into JPG files, and overlapped with the DAPI channel. In order to avoid potential background segmentation, only nuclei containing masks for each respective channel were manually counted and considered positive for each one of them. Ratios of D1R to D2R positive cells were calculated and compared between injected and non-injected hemispheres to quantify SPN loss in the striatum.

Acute slice electrophysiology

Mice were anesthetized with isoflurane and transcardially perfused with ~5 mL of ice-cold artificial cerebrospinal fluid (ACSF, in mM): 25 $NaHCO_3$, 125 NaCl, 1.25 NaH_2PO_4 monohydrate, 2.5 KCl, 12.5 D-glucose, 1 $MgCl_2$ hexahydrate, and 2 $CaCl_2$ (on average 307.3 mOsm/kg). Upon decapitation, brains were extracted and placed on an ACSF-soaked filter paper, cerebellum was severed, and hemispheres were carefully bisected with a razor blade. The exposed posterior surface was glued to a magnetic chuck and secured in the cutting chamber containing ice-cold ACSF continuously equilibrated with carbogen (95% O_2/5% CO_2) and surrounded by ice. Sections containing dmPFC were cut at 275 µm (0.12 mm/s) using a vibratome (VT 2000, Leica) and incubated for 10-15 min at 32°C in a choline chloride solution containing (in mM): 25 $NaHCO_3$, 1.25 NaH_2PO_4 monohydrate, 12.5 D-glucose, 2.5 KCl, 7 $MgCl_2$ hexahydrate, 0.5 $CaCl_2$, 110 choline chloride, 11.6 ascorbic acid, and 3.1 pyruvic acid. Sections recovered for 45 min in ACSF preheated to 32°C and gradually returned to 20-22°C. Individual sections were transferred to a recording chamber attached to an upright microscope (Scientifica) and continuously perfused at 2-2.5 mL/min with equilibrated ACSF at 20-22°C. Pump-recirculated ACSF bath contained 10mM RS-CPP to abolish NMDAR-mediated currents and 1mM TTX to prevent voltage dependent sodium channel currents. To patch cells, we pulled (P-1000, 2.5x2.5 mm box filament, Sutter Instruments) pipettes from thick-walled, filamented borosilicate glass (OD 1.5 mm, ID 0.86 mm, Sutter Instruments) with resistance 2.5-3.5 MΩ when filled with the internal solution and positive pressure. To facilitate space-clamp, we filled pipettes with a cesium methanesulfonate-based solution containing (in mM): 130 $CsMeSO_3$, 10 HEPES, 1.8 $MgCl_2$ hydroxide, 8 sodium phosphocreatine, 10 CsCl, 3.3 QX 314 (Cl^- salt), 4 disodium ATP, and 0.3 sodium GTP (pH adjusted to 7.3 with CsOH, 299 mOsm/kg). Morphology was visualized by adding 0.7 µL of Alexa Fluor 488 hydrazide (Thermo Fisher, A10436) dissolved in water (1:100) to the internal solution that was kept on ice and dispensed through a microfil tip coupled to a 0.22 µm filter (Millipore). We targeted L2/3 cells located 150-250 µm from the medial surface, and upon forming a 2-3 GΩ seal, broke into whole-cell configuration, immediately recording intrinsic properties. Cells were voltage clamped at V_h = -70mV and perfused with internal solution for 4 minutes after which mEPSCs were acquired for 5 minutes. At the end of each 10 second sweep, a test pulse injection continuously monitored

input (R_{in}) and series (R_s) resistance. In order to assay inhibitory currents mediated by $GABA_A$/glycine receptors, the same cell was clamped at V_h = 0mV, allowed to stabilize for 1 minute, and mIPSCs were acquired for 5 minutes. Currents were amplified by MultiClamp 700B (Molecular Devices), low-pass Bessel filtered at 3 kHz, digitized at 10 kHz, and acquired in ScanImage program running in MATLAB 2019a (Mathworks) and relayed by TeleConverter. Each cell recording was concluded by noting the final Rs and the presence of putative spines and an apical dendrite were confirmed by imaging (470nm, pE-300, CoolLED) the intracellular Alexa Fluor 488 signal. A 4x DIC image of the cell location in the section was obtained to confirm location in ipsilateral L2/3 dmPFC. Cells were included in analysis if they exhibited 1) initial R_s < 20 MΩ, 2) final R_s < 25 MΩ, 3) R_{in} > 100 MΩ, 4) V_h = -70 or 0 mV requiring < 100 pA, 5) fluorescently labeled putative spines, 6) a distinct apical dendrite, and 7) excitatory inputs decaying to tau in > 4 ms.

Analysis of electrophysiology data

To identify miniature postsynaptic currents, sweeps were analyzed using the open-source program Clampsuite (https://github.com/LarsHenrikNelson/ClampSuite). Sweeps were processed using a zero-phase finite impulse response filter (order = 201, window = 150 samples) with a low pass cutoff at 450 Hz. To automatically identify events, filtered sweeps were deconvolved from a predefined mEPSC or mIPSC template using Fast Fourier Transform and inverted. Specifically, mIPSCs had to satisfy 1) peak amplitude > 6 pA, 2) rise time 0.5-4 ms, and 3) decay time > 4 ms, whereas mEPSCs had to satisfy 1) peak amplitude > 7 pA, 2) rise time 0.5-4 ms, and 3) decay time > 4 ms. Decay time was defined as time to tau, given by peak amplitude divided by 1/*e*. Every identified event was inspected manually. In some cases, mIPSC events were missed by the program and were manually included if they met the above criteria.

References

1. Shepherd, G. M. G. Corticostriatal connectivity and its role in disease. *Nat Rev Neurosci* **14,** 278–91 (2013).
2. Hintiryan, H., Foster, N. N., Bowman, I., Bay, M., Song, M. Y., Gou, L., Yamashita, S., Bienkowski, M. S., Zingg, B., Zhu, M., Yang, X. W., Shih, J. C., Toga, A. W. & Dong, H. W. The mouse cortico-striatal projectome. *Nat Neurosci* (2016). doi:10.1038/nn.4332
3. Foster, N. N., Barry, J., Korobkova, L., Garcia, L., Gao, L., Becerra, M., Sherafat, Y., Peng, B., Li, X., Choi, J. H., Gou, L., Zingg, B., Azam, S., Lo, D., Khanjani, N., Zhang, B., Stanis, J., Bowman, I., Cotter, K., Cao, C., Yamashita, S., Tugangui, A., Li, A., Jiang, T., Jia, X., Feng, Z., Aquino, S., Mun, H. S., Zhu, M., Santarelli, A., Benavidez, N. L., Song, M., Dan, G., Fayzullina, M., Ustrell, S., Boesen, T., Johnson, D. L., Xu, H., Bienkowski, M. S., Yang, X. W., Gong, H., Levine, M. S., Wickersham, I., Luo, Q., Hahn, J. D., Lim, B. K., Zhang, L. I., Cepeda, C., Hintiryan, H. & Dong, H. W. The mouse cortico–basal ganglia–thalamic network. *Nature* (2021). doi:10.1038/s41586-021-03993-3

4. Oldenburg, I. A. & Sabatini, B. L. Antagonistic but Not Symmetric Regulation of Primary Motor Cortex by Basal Ganglia Direct and Indirect Pathways. *Neuron* **86,** 1174–1181 (2015).
5. Djurfeldt, M., Ekeberg, Ö. & Graybiel, A. M. Cortex-basal ganglia interaction and attractor states. *Neurocomputing* **38–40,** 573–579 (2001).
6. Lee, H. J., Weitz, A. J., Bernal-Casas, D., Duffy, B. A., Choy, M. K., Kravitz, A. V., Kreitzer, A. C. & Lee, J. H. Activation of Direct and Indirect Pathway Medium Spiny Neurons Drives Distinct Brain-wide Responses. *Neuron* (2016). doi:10.1016/j.neuron.2016.06.010
7. Poulet, J. F. A., Fernandez, L. M. J., Crochet, S. & Petersen, C. C. H. Thalamic control of cortical states. *Nat Neurosci* (2012). doi:10.1038/nn.3035
8. Saalmann, Y. B., Pinsk, M. A., Wang, L., Li, X. & Kastner, S. The pulvinar regulates information transmission between cortical areas based on attention demands. *Science (1979)* (2012). doi:10.1126/science.1223082
9. Steriade, M., Contreras, D., Amzica, F. & Timofeev, I. Synchronization of fast (30-40 Hz) spontaneous oscillations in intrathalamic and thalamocortical networks. *Journal of Neuroscience* (1996). doi:10.1523/jneurosci.16-08-02788.1996
10. Fiebelkorn, I. C., Pinsk, M. A. & Kastner, S. The mediodorsal pulvinar coordinates the macaque fronto-parietal network during rhythmic spatial attention. *Nat Commun* (2019). doi:10.1038/s41467-018-08151-4
11. Martini, F. J., Guillamón-Vivancos, T., Moreno-Juan, V., Valdeolmillos, M. & López-Bendito, G. Spontaneous activity in developing thalamic and cortical sensory networks. *Neuron* **109,** 2519–2534 (2021).
12. Peixoto, R. T., Wang, W., Croney, D. M., Kozorovitskiy, Y., Sabatini, B. L. & Peixoto, R, Wang, W, Croney, D, Kozorovitskiy, Y, Sabatini, B. Early hyperactivity and precocious maturation of corticostriatal circuits in Shank3B-/- mice. *Nat Neurosci* **19,** 716–24 (2016).
13. Kozorovitskiy, Yevgenia, Peixoto, Rui, Saunders, Arpiar, Sabatini, B. Neuromodulation of excitatory synaptogenesis in striatal development. (2015). doi:10.7554/eLife.10111
14. Peixoto, R. T., Chantranupong, L., Hakim, R., Levasseur, J., Wang, W., Merchant, T., Gorman, K., Budnik, B. & Sabatini, B. L. Abnormal Striatal Development Underlies the Early Onset of Behavioral Deficits in Shank3B−/− Mice. *Cell Rep* (2019). doi:10.1016/j.celrep.2019.10.021
15. Kreitzer, A. C. & Malenka, R. C. Striatal Plasticity and Basal Ganglia Circuit Function. *Neuron* **60,** 543–554 (2008).
16. Monosov, I. E., Haber, S. N., Leuthardt, E. C. & Jezzini, A. Anterior Cingulate Cortex and the Control of Dynamic Behavior in Primates. *Current Biology* **30,** R1442–R1454 (2020).
17. Reiner, A. Corticostriatal projection neurons – dichotomous types and dichotomous functions. *Front Neuroanat* **4,** 1–15 (2010).
18. Bosch-Bouju, C., Hyland, B. I. & Parr-Brownlie, L. C. Motor thalamus integration of cortical, cerebellar and basal ganglia information: implications for normal and parkinsonian conditions. *Front Comput Neurosci* **7,** (2013).
19. Tanibuchi, I., Kitano, H. & Jinnai, K. Substantia Nigra Output to Prefrontal Cortex Via Thalamus in Monkeys. I. Electrophysiological Identification of Thalamic Relay Neurons. *J Neurophysiol* **102,** 2933–2945 (2009).
20. Haber, S. N. & Calzavara, R. The cortico-basal ganglia integrative network: The role of the thalamus. *Brain Res Bull* Preprint at https://doi.org/10.1016/j.brainresbull.2008.09.013 (2009)
21. McFarland, N. R. & Haber, S. N. Thalamic Relay Nuclei of the Basal Ganglia Form Both Reciprocal and Nonreciprocal Cortical Connections, Linking Multiple Frontal Cortical Areas. *The Journal of Neuroscience* **22,** 8117–8132 (2002).

22. Lalive, A. L., Lien, A. D., Roseberry, T. K., Donahue, C. H. & Kreitzer, A. C. Motor thalamus supports striatum-driven reinforcement. *Elife* **7,** (2018).
23. Parnaudeau, S., Bolkan, S. S. & Kellendonk, C. The Mediodorsal Thalamus: An Essential Partner of the Prefrontal Cortex for Cognition. *Biol Psychiatry* **83,** 648–656 (2018).
24. Mukherjee, A., Lam, N. H., Wimmer, R. D. & Halassa, M. M. Thalamic circuits for independent control of prefrontal signal and noise. *Nature* **600,** 100–104 (2021).
25. Roy, D. S., Zhang, Y., Halassa, M. M. & Feng, G. Thalamic subnetworks as units of function. *Nat Neurosci* **25,** 140–153 (2022).
26. Rubenstein, J. L. R. & Merzenich, M. M. Model of autism: increased ratio of excitation/inhibition in key neural systems. *Genes Brain Behav* **2,** 255–267 (2003).
27. Marín, O. Interneuron dysfunction in psychiatric disorders. *Nat Rev Neurosci* **13,** 107–20 (2012).
28. Gao, R. & Penzes, P. Common Mechanisms of Excitatory and Inhibitory Imbalance in Schizophrenia and Autism Spectrum Disorders. *Curr Mol Med* **15,** 146–167 (2015).
29. Sohal, V. S. & Rubenstein, J. L. R. Excitation-inhibition balance as a framework for investigating mechanisms in neuropsychiatric disorders. *Mol Psychiatry* **24,** 1248–1257 (2019).
30. Narboux-Nême, N., Evrard, A., Ferezou, I., Erzurumlu, R. S., Kaeser, P. S., Lainé, J., Rossier, J., Ropert, N., Südhof, T. C. & Gaspar, P. Neurotransmitter release at the thalamocortical synapse instructs barrel formation but not axon patterning in the somatosensory cortex. *Journal of Neuroscience* (2012). doi:10.1523/JNEUROSCI.0343-12.2012
31. Li, H., Fertuzinhos, S., Mohns, E., Hnasko, T. S., Verhage, M., Edwards, R., Sestan, N. & Crair, M. C. Laminar and Columnar Development of Barrel Cortex Relies on Thalamocortical Neurotransmission. *Neuron* (2013). doi:10.1016/j.neuron.2013.06.043
32. Pouchelon, G., Gambino, F., Bellone, C., Telley, L., Vitali, I., Lüscher, C., Holtmaat, A. & Jabaudon, D. Modality-specific thalamocortical inputs instruct the identity of postsynaptic L4 neurons. *Nature* (2014). doi:10.1038/nature13390
33. Rakic, P. Specification of cerebral cortical areas. *Science (1979)* (1988). doi:10.1126/science.3291116
34. Innocenti, G. M. & Price, D. J. Exuberance in the development of cortical networks. *Nat Rev Neurosci* Preprint at https://doi.org/10.1038/nrn1790 (2005)
35. Price, D. J., Kennedy, H., Dehay, C., Zhou, L., Mercier, M., Jossin, Y., Goffinet, A. M., Tissir, F., Blakey, D. & Molnár, Z. The development of cortical connections. *European Journal of Neuroscience* Preprint at https://doi.org/10.1111/j.1460-9568.2006.04620.x (2006)
36. Marín, O. Interneuron dysfunction in psychiatric disorders. *Nat Rev Neurosci* **13,** 107–20 (2012).
37. Canetta, S. E., Holt, E. S., Benoit, L. J., Teboul, E., Sahyoun, G. M., Ogden, R. T., Harris, A. Z. & Kellendonk, C. Mature parvalbumin interneuron function in prefrontal cortex requires activity during a postnatal sensitive period. *Elife* **11,** (2022).
38. Benoit, L. J., Holt, E. S., Posani, L., Fusi, S., Harris, A. Z., Canetta, S. & Kellendonk, C. Adolescent thalamic inhibition leads to long-lasting impairments in prefrontal cortex function. *Nat Neurosci* **25,** 714–725 (2022).
39. Hensch, T. K. Critical period plasticity in local cortical circuits. *Nat Rev Neurosci* **6,** 877–88 (2005).
40. Hensch, T. K., Fagiolini, M., Mataga, N., Stryker, M. P., Baekkeskov, S. & Kash, S. F. Local GABA Circuit Control of Experience-Dependent Plasticity in Developing Visual Cortex. *Science (1979)* **282,** 1504–1508 (1998).

41. Lazarus, M. S. & Huang, Z. J. Distinct maturation profiles of perisomatic and dendritic targeting GABAergic interneurons in the mouse primary visual cortex during the critical period of ocular dominance plasticity. *J Neurophysiol* **106,** 775–787 (2011).
42. Chittajallu, R. & Isaac, J. T. R. Emergence of cortical inhibition by coordinated sensory-driven plasticity at distinct synaptic loci. *Nat Neurosci* **13,** 1240–1248 (2010).
43. Kirkby, L. A., Sack, G. S., Firl, A. & Feller, M. B. A role for correlated spontaneous activity in the assembly of neural circuits. *Neuron* **80,** 1129–44 (2013).
44. Colonnese, M. T., Kaminska, A., Minlebaev, M., Milh, M., Bloem, B., Lescure, S., Moriette, G., Chiron, C., Ben-Ari, Y. & Khazipov, R. A Conserved Switch in Sensory Processing Prepares Developing Neocortex for Vision. *Neuron* **67,** 480–498 (2010).
45. Khazipov, R., Sirota, A., Leinekugel, X., Holmes, G. L., Ben-Ari, Y. & Buzsáki, G. Early motor activity drives spindle bursts in the developing somatosensory cortex. *Nature* **432,** 758–761 (2004).
46. Shen, J. & Colonnese, M. T. Development of Activity in the Mouse Visual Cortex. *Journal of Neuroscience* (2016). doi:10.1523/JNEUROSCI.1903-16.2016
47. Chini, M., Pfeffer, T. & Hanganu-Opatz, I. An increase of inhibition drives the developmental decorrelation of neural activity. *Elife* **11,** (2022).
48. Bitzenhofer, S. H., Pöpplau, J. A. & Hanganu-Opatz, I. Gamma activity accelerates during prefrontal development. *Elife* **9,** (2020).
49. Anastasiades, P. G., Collins, D. P. & Carter, A. G. Mediodorsal and Ventromedial Thalamus Engage Distinct L1 Circuits in the Prefrontal Cortex. *Neuron* **109,** 314-330.e4 (2021).
50. Collins, D. P., Anastasiades, P. G., Marlin, J. J. & Carter, A. G. Reciprocal Circuits Linking the Prefrontal Cortex with Dorsal and Ventral Thalamic Nuclei. *Neuron* **98,** 366-379.e4 (2018).
51. Delevich, K., Tucciarone, J., Huang, Z. J. & Li, B. The mediodorsal thalamus drives feedforward inhibition in the anterior cingulate cortex via parvalbumin interneurons. *Journal of Neuroscience* **35,** 5743–5753 (2015).
52. Mowery, T. M., Penikis, K. B., Young, S. K., Ferrer, C. E., Kotak, V. C. & Sanes, D. H. The Sensory Striatum Is Permanently Impaired by Transient Developmental Deprivation. *Cell Rep* **19,** 2462–2468 (2017).
53. Medendorp, W. E., Bjorefeldt, A., Crespo, E. L., Prakash, M., Pal, A., Waddell, M. L., Moore, C. I. & Hochgeschwender, U. Selective postnatal excitation of neocortical pyramidal neurons results in distinctive behavioral and circuit deficits in adulthood. *iScience* **24,** 102157 (2021).
54. Kozorovitskiy, Y., Saunders, A., Johnson, C. A., Lowell, B. B. & Sabatini, B. L. Recurrent network activity drives striatal synaptogenesis. *Nature* **485,** 646–650 (2012).
55. Murata, Y. & Colonnese, M. T. Thalamus controls development and expression of arousal states in visual cortex. *Journal of Neuroscience* (2018). doi:10.1523/JNEUROSCI.1519-18.2018
56. Gong, S., Doughty, M., Harbaugh, C. R., Cummins, A., Hatten, M. E., Heintz, N. & Gerfen, C. R. Targeting Cre Recombinase to Specific Neuron Populations with Bacterial Artificial Chromosome Constructs. *The Journal of Neuroscience* **27,** 9817–9823 (2007).
57. Fentress, J. C., Stanfield, B. B. & Cowan, W. M. Observations on the development of the striatum in mice and rats. *Anat Embryol (Berl)* (1981). doi:10.1007/BF00315705
58. Sreenivasan, V., Serafeimidou-Pouliou, E., Exposito-Alonso, D., Bercsenyi, K., Bernard, C., Bae, S.-E., Oozeer, F., Hanusz-Godoy, A., Edwards, R. H. & Marín, O. Input-specific control of interneuron numbers in nascent striatal networks. *Proceedings of the National Academy of Sciences* **119,** (2022).

59. Pachitariu, M., Stringer, C., Dipoppa, M., Schröder, S., Rossi, L. F., Dalgleish, H., Carandini, M. & Harris, K. Suite2p: beyond 10,000 neurons with standard two-photon microscopy. *bioRxiv* 061507 (2016). doi:10.1101/061507
60. Wolff, J. J., Hazlett, H. C., Lightbody, A. a, Reiss, A. L. & Piven, J. Repetitive and self-injurious behaviors: associations with caudate volume in autism and fragile X syndrome. *J Neurodev Disord* **5,** 12 (2013).
61. Turner, K. C., Frost, L., Linsenbardt, D., McIlroy, J. R. & Müller, R.-A. Atypically diffuse functional connectivity between caudate nuclei and cerebral cortex in autism. *Behav Brain Funct* **2,** 34 (2006).
62. Langen, M., Bos, D., Noordermeer, S. D. S., Nederveen, H., Van Engeland, H. & Durston, S. Changes in the development of striatum are involved in repetitive behavior in autism. *Biol Psychiatry* **76,** 405–411 (2014).
63. Langen, M., Schnack, H. G., Nederveen, H., Bos, D., Lahuis, B. E., de Jonge, M. V., van Engeland, H. & Durston, S. Changes in the Developmental Trajectories of Striatum in Autism. *Biol Psychiatry* **66,** 327–333 (2009).
64. Langen, M., Durston, S., Staal, W. G., Palmen, S. J. M. C. & van Engeland, H. Caudate Nucleus Is Enlarged in High-Functioning Medication-Naive Subjects with Autism. *Biol Psychiatry* **62,** 262–266 (2007).
65. Fuccillo, M. V. Striatal Circuits as a Common Node for Autism Pathophysiology. *Front Neurosci* **10,** 27 (2016).
66. Benthall, K. N., Ong, S. L. & Bateup, H. S. Corticostriatal Transmission Is Selectively Enhanced in Striatonigral Neurons with Postnatal Loss of Tsc1. *Cell Rep* **23,** 3197–3208 (2018).
67. Wang, W., Li, C., Chen, Q., Van Der Goes, M. S., Hawrot, J., Yao, A. Y., Gao, X., Lu, C., Zang, Y., Zhang, Q., Lyman, K., Wang, D., Guo, B., Wu, S., Gerfen, C. R., Fu, Z. & Feng, G. Striatopallidal dysfunction underlies repetitive behavior in Shank3-deficient model of autism. *Journal of Clinical Investigation* (2017). doi:10.1172/JCI87997
68. Rothwell, P. E., Fuccillo, M. V., Maxeiner, S., Hayton, S. J., Gokce, O., Lim, B. K., Fowler, S. C., Malenka, R. C. & Südhof, T. C. Autism-Associated Neuroligin-3 Mutations Commonly Impair Striatal Circuits to Boost Repetitive Behaviors. *Cell* **158,** 198–212 (2014).
69. Wilson, C. J. Active decorrelation in the basal ganglia. *Neuroscience* **250,** 467–482 (2013).
70. Nevet, A., Morris, G., Saban, G., Arkadir, D. & Bergman, H. Lack of spike-count and spike-time correlations in the substantia nigra reticulata despite overlap of neural responses. *J Neurophysiol* **98,** 2232–2243 (2007).
71. Gittis, A. H. & Kreitzer, A. C. Striatal microcircuitry and movement disorders. *Trends Neurosci* Preprint at https://doi.org/10.1016/j.tins.2012.06.008 (2012)
72. Uhlhaas, P. J. & Singer, W. Neural Synchrony in Brain Disorders: Relevance for Cognitive Dysfunctions and Pathophysiology. *Neuron* **52,** 155–168 (2006).
73. Smith, Y., Galvan, A., Ellender, T. J., Doig, N., Villalba, R. M., Huerta-Ocampo, I., Wichmann, T. & Bolam, J. P. The thalamostriatal system in normal and diseased states. *Front Syst Neurosci* **8,** 5 (2014).
74. Hammond, C., Bergman, H. & Brown, P. Pathological synchronization in Parkinson's disease: networks, models and treatments. *Trends Neurosci* **30,** 357–364 (2007).
75. Gainey, M. A. & Feldman, D. E. Multiple shared mechanisms for homeostatic plasticity in rodent somatosensory and visual cortex. *Philosophical Transactions of the Royal Society B: Biological Sciences* **372,** 20160157 (2017).
76. Hartley, C. A., Nussenbaum, K. & Cohen, A. O. Interactive Development of Adaptive Learning and Memory. *Annu Rev Dev Psychol* **3,** 59–85 (2021).

77. Neely, R. M., Koralek, A. C., Athalye, V. R., Costa, R. M. & Carmena, J. M. Volitional Modulation of Primary Visual Cortex Activity Requires the Basal Ganglia. *Neuron* **97,** 1356-1368.e4 (2018).
78. Wang, J. X., Kurth-Nelson, Z., Kumaran, D., Tirumala, D., Soyer, H., Leibo, J. Z., Hassabis, D. & Botvinick, M. Prefrontal cortex as a meta-reinforcement learning system. *Nat Neurosci* **21,** 860–868 (2018).

Figure 1

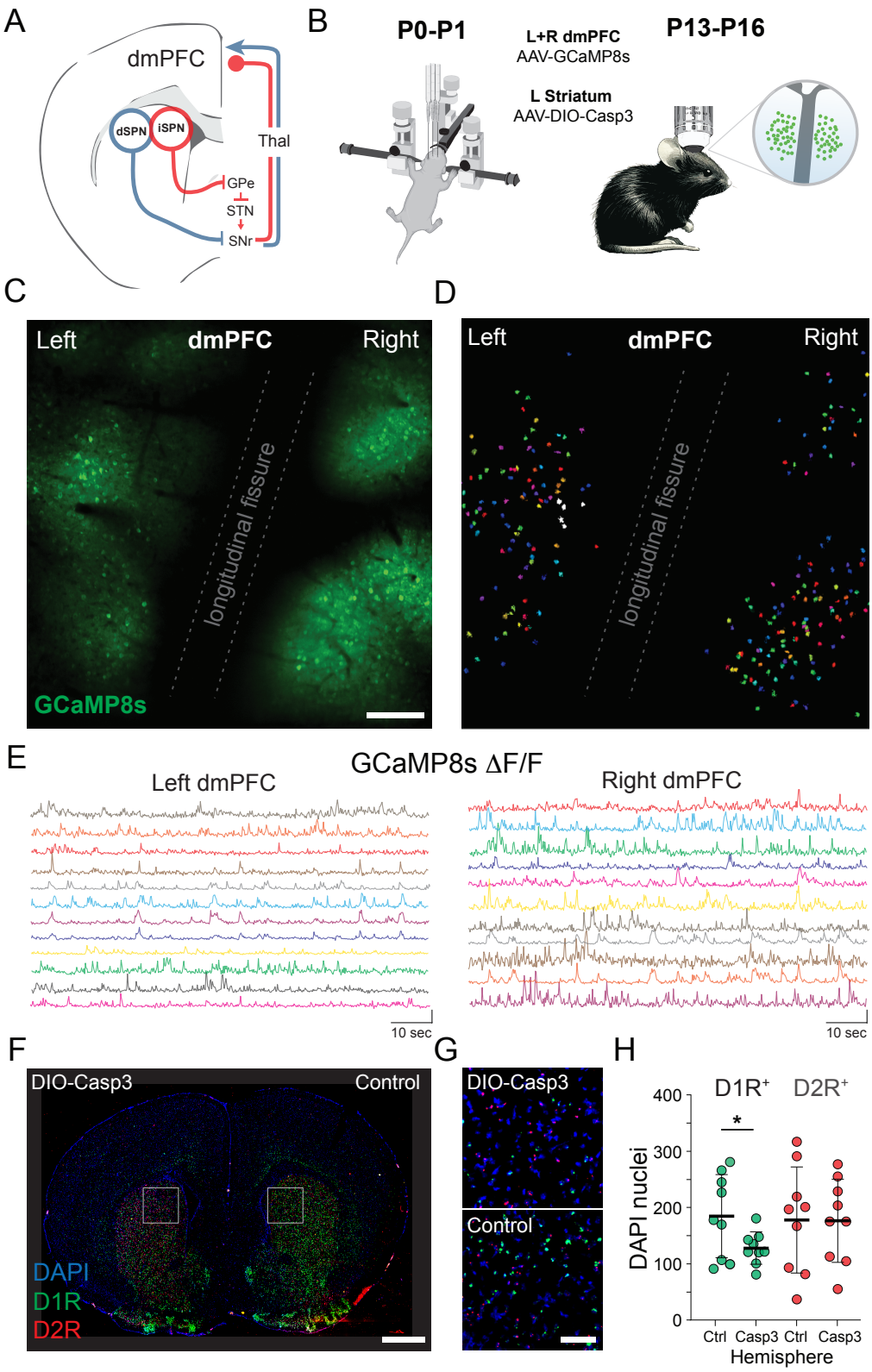
A
dmPFC
dSPN
iSPN
Thal
GPe
STN
SNr
B
P0-P1
L+R dmPFC
AAV-GCaMP8s
L Striatum
AAV-DIO-Casp3
P13-P16
C
Left
dmPFC
Right
longitudinal fissure
GCaMP8s
D
Left
dmPFC
Right
longitudinal fissure
E
GCaMP8s ΔF/F
Left dmPFC
Right dmPFC
10 sec
10 sec
F
DIO-Casp3
Control
DAPI
D1R
D2R
G
DIO-Casp3
Control
H
D1R+
D2R+
*
DAPI nuclei
400
300
200
100
0
Ctrl
Casp3
Ctrl
Casp3
Hemisphere

Figure 2

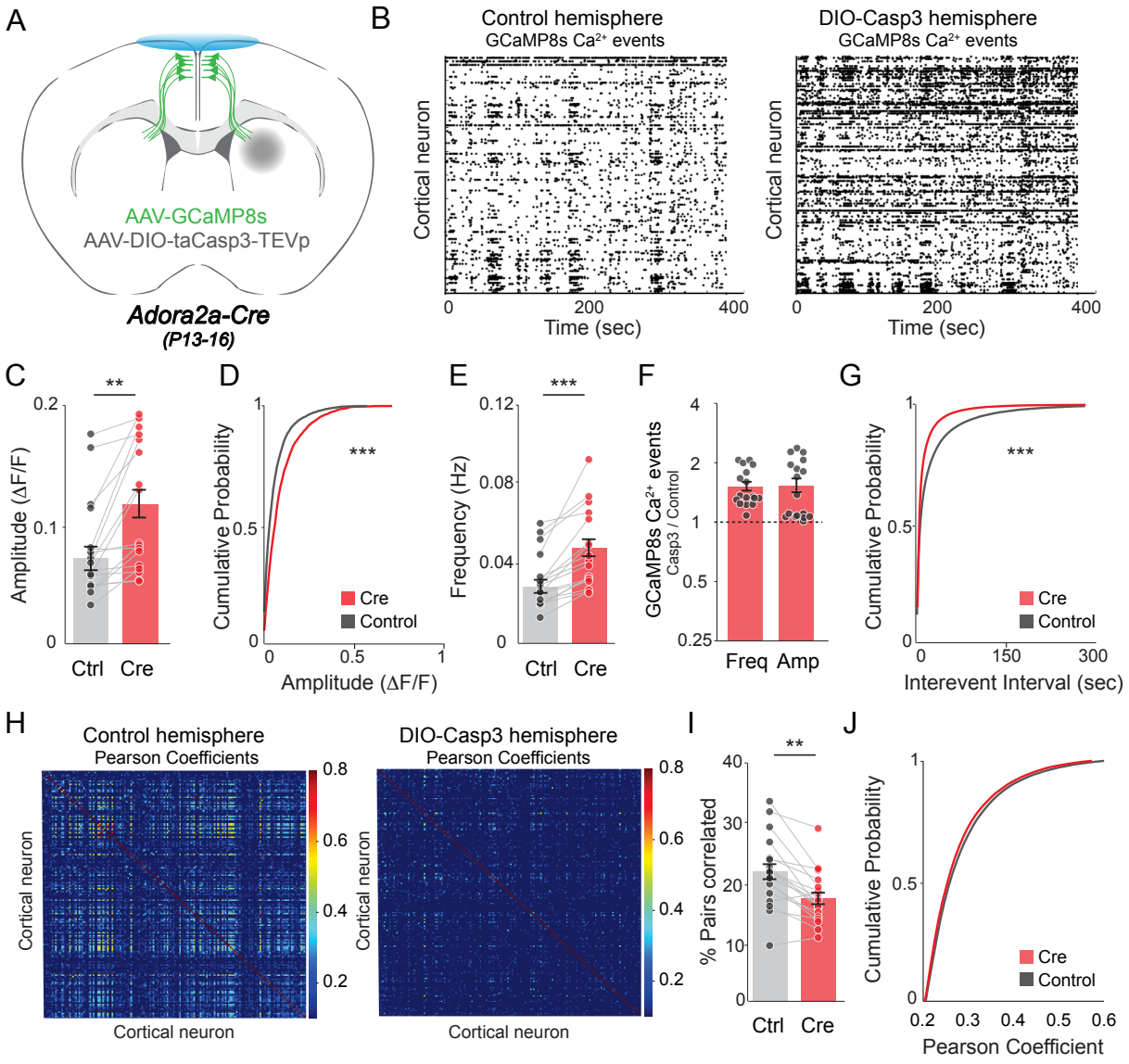
A
AAV-GCaMP8s
AAV-DIO-taCasp3-TEVp
Adora2a-Cre
(P13-16)
B
Control hemisphere
GCaMP8s Ca2+ events
DIO-Casp3 hemisphere
GCaMP8s Ca2+ events
Cortical neuron
Time (sec)
C
Amplitude (ΔF/F)
Ctrl
Cre
D
Cumulative Probability
Amplitude (ΔF/F)
Cre
Control
E
Frequency (Hz)
Ctrl
Cre
F
GCaMP8s Ca2+ events
Casp3 / Control
Freq
Amp
G
Cumulative Probability
Interevent Interval (sec)
Cre
Control
H
Control hemisphere
Pearson Coefficients
DIO-Casp3 hemisphere
Pearson Coefficients
Cortical neuron
I
% Pairs correlated
Ctrl
Cre
J
Cumulative Probability
Pearson Coefficient
Cre
Control

Figure 3

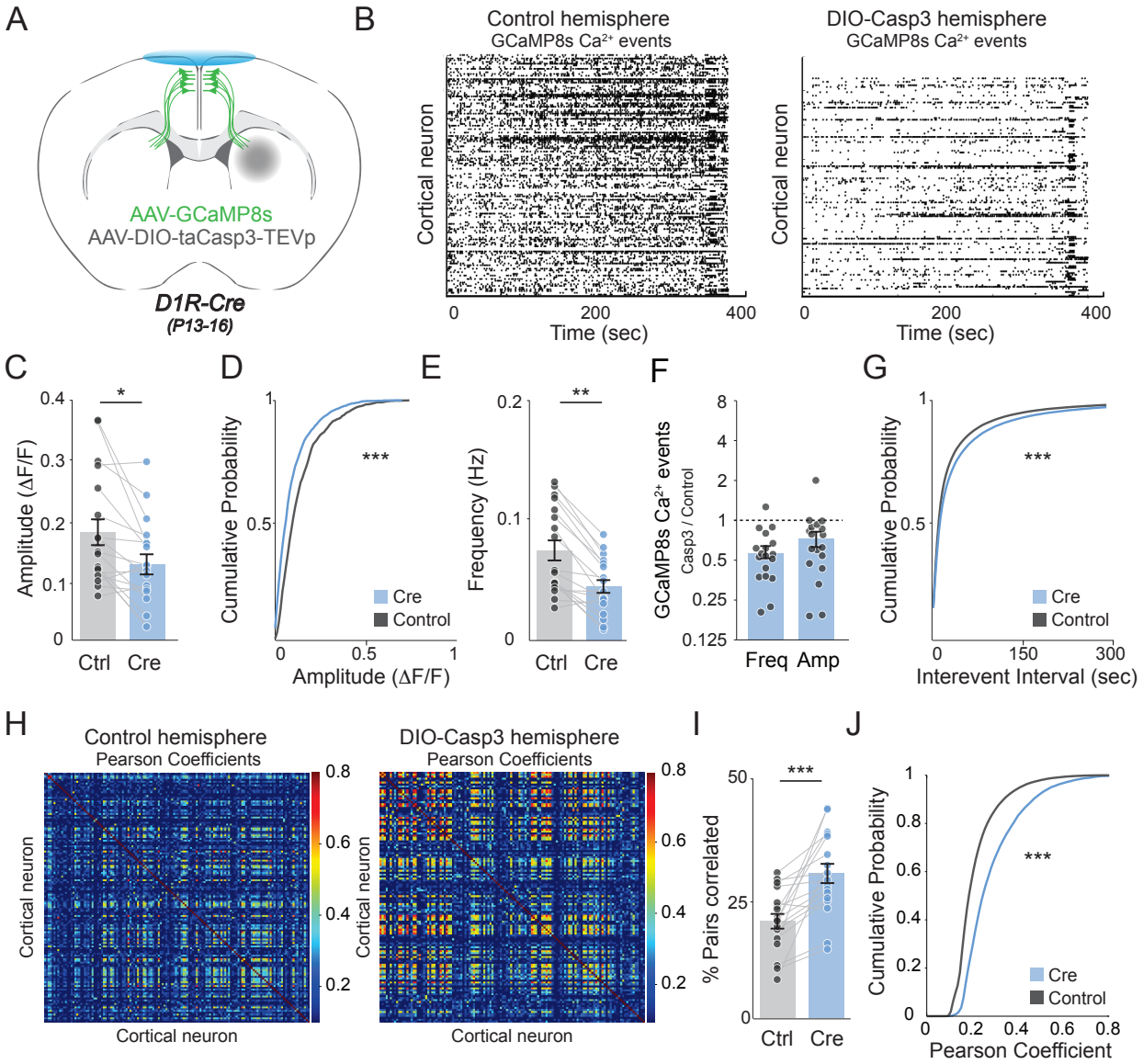
A
AAV-GCaMP8s
AAV-DIO-taCasp3-TEVp
D1R-Cre
(P13-16)
B
Control hemisphere
GCaMP8s Ca2+ events
DIO-Casp3 hemisphere
GCaMP8s Ca2+ events
Cortical neuron
Time (sec)
C
Amplitude (ΔF/F)
Ctrl
Cre
D
Cumulative Probability
Amplitude (ΔF/F)
Cre
Control
E
Frequency (Hz)
F
GCaMP8s Ca2+ events
Casp3 / Control
Freq
Amp
G
Interevent Interval (sec)
H
Control hemisphere
Pearson Coefficients
DIO-Casp3 hemisphere
Pearson Coefficients
Cortical neuron
I
% Pairs correlated
J
Pearson Coefficient

Figure 4

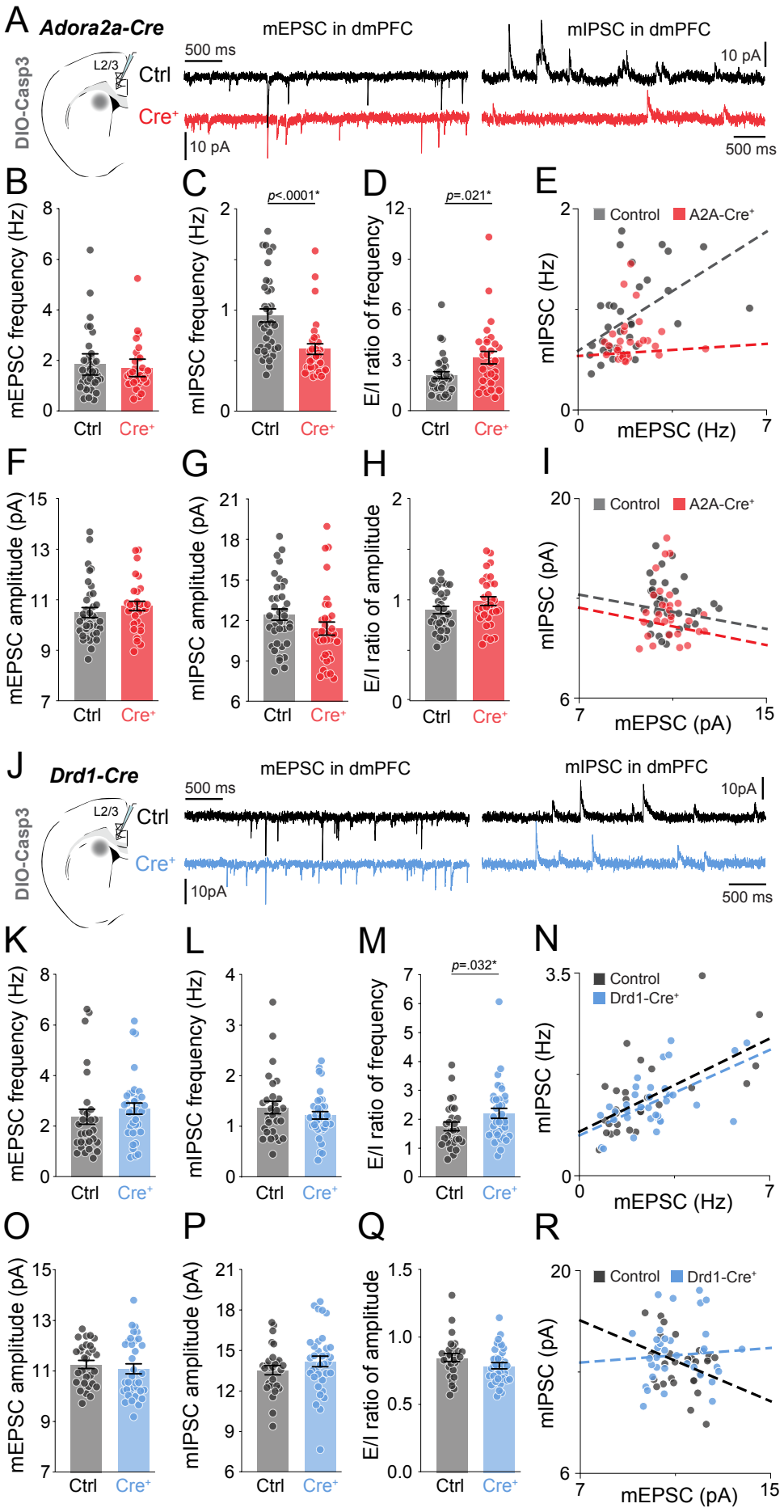
A
Adora2a-Cre
DIO-Casp3
L2/3
Ctrl
Cre+
mEPSC in dmPFC
mIPSC in dmPFC
500 ms
10 pA
B
mEPSC frequency (Hz)
C
mIPSC frequency (Hz)
p<.0001*
D
E/I ratio of frequency
p=.021*
E
Control
A2A-Cre+
mIPSC (Hz)
mEPSC (Hz)
F
mEPSC amplitude (pA)
G
mIPSC amplitude (pA)
H
E/I ratio of amplitude
I
mIPSC (pA)
mEPSC (pA)
J
Drd1-Cre
10pA
K
L
M
p=.032*
N
Drd1-Cre+
O
P
Q
R